

Supporting Information:
Quantum Spectral Engineering for Enhanced Agrivoltaic Efficiency:
Non-Markovian Dynamics in Photosynthetic Energy Transfer

Steve Cabrel Teguia Kouam^{2,*}, Theodore Goumai Vedekoi¹, Jean-Pierre Tchapet Njafa¹,
Jean-Pierre Nguenang², Serge Guy Nana Engo¹

¹Department of Physics, Faculty of Science, University of Yaoundé I, Cameroon

²Department of Physics, Faculty of Science, University of Douala, Cameroon

*Corresponding author: steve.teguia@univ-douala.cm

February 19, 2026

Contents

1 Environmental factor models	3
1.1 Solar spectral modeling	3
1.1.1 Reference spectrum (AM1.5G)	3
1.1.2 Geographic variations	3
1.1.3 Seasonal and diurnal variations	3
1.2 Atmospheric effects	3
1.2.1 Aerosol optical depth (AOD)	3
1.2.2 Water vapor absorption	4
1.2.3 Cloud cover and diffuse radiation	4
1.3 Dust and soiling effects	4
1.3.1 Particle accumulation model	4
1.3.2 Spectral selectivity of soiling	4
1.4 Weather modelling	4
1.5 Integration with quantum simulations	4
2 Biodegradability assessment	4
2.1 Fukui function analysis	5
2.1.1 Theoretical framework	5
2.1.2 Computational details	5
2.2 Global reactivity descriptors	5
2.2.1 Chemical hardness and softness	5
2.2.2 Electrophilicity index	5
2.2.3 Nucleophilicity index	5
2.3 Enzymatic degradation pathways	6
2.3.1 Hydrolase attack (ester linkages)	6
2.3.2 Oxidase attack (aromatic rings)	6
2.3.3 Bond dissociation energies	6
2.4 Biodegradability index	6

3	Extended validation data	6
3.1	FMO complex Hamiltonian	7
3.2	Convergence tests (tests 1–4)	7
3.2.1	Test 1: HEOM benchmark	7
3.2.2	Test 2: Matsubara cutoff convergence	7
3.2.3	Test 3: Time step convergence	7
3.2.4	Test 4: Hierarchy truncation convergence	7
3.3	Physical consistency tests (tests 5–8)	8
3.3.1	Test 5: Trace preservation	8
3.3.2	Test 6: Positivity	8
3.3.3	Test 7: Energy conservation	8
3.3.4	Test 8: Detailed balance	8
3.4	Environmental robustness tests (tests 9–12)	8
3.4.1	Test 9: Temperature sensitivity	8
3.4.2	Test 10: Static disorder	8
3.4.3	Test 11: Bath parameter variations	8
3.4.4	Test 12: Markovian limit recovery	8
3.5	Summary of validation results	8
4	Complete FMO parameter sets	8
4.1	Site energies (Adolphs & Renger, 2006)	8
4.2	Electronic couplings	9
4.3	Spectral density parameters	9
5	Process Tensor-HOPS with low-temperature correction	10
5.1	Padé decomposition of the bath correlation function	10
5.2	Low-temperature correction parameters	10
6	Computational performance metrics	11
6.1	Hardware specifications	11
6.2	Scaling analysis	11
6.3	Parallelization efficiency	11
7	Additional figures	11
7.1	Figure S1: Spectral density components	11
7.2	Figure S2: Quantum metrics evolution	12
7.3	Figure S3: Global reactivity indices	12
7.4	Figure S4: PAR transmission (clean vs dusty)	12
7.5	Figure S5: Response functions	12
7.6	Figure S6: Geographic climate maps	12
7.7	Figure S7: ETR uncertainty distributions	12
7.8	Figure S8: Sub-Saharan Africa ETR enhancement	12

1 Environmental factor models

This section details the environmental factor models used to assess the applicability of quantum-optimized agrivoltaic systems across diverse geographic and climatic conditions. These models underpin the geographic simulations reported in Section 3 of the main text.

1.1 Solar spectral modeling

1.1.1 Reference spectrum (AM1.5G)

The baseline solar spectral irradiance follows the ASTM G173-03 reference standard (Air Mass 1.5 Global tilted):

$$J_{\text{solar}}^{\text{ref}}(\lambda) = J_{\text{AM1.5G}}(\lambda) \quad \text{for } \lambda \in 280 \text{ nm to } 4000 \text{ nm}, \quad (1)$$

with integrated power density $P_{\text{total}} = \int J_{\text{solar}}^{\text{ref}}(\lambda) d\lambda = 1000 \text{ W m}^{-2}$.

Photosynthetically active radiation (PAR) spans 400 nm to 700 nm, representing approximately 45 % of total solar energy (450 W m^{-2}).

1.1.2 Geographic variations

Solar spectra vary by latitude due to atmospheric path length differences. We model this using Beer–Lambert attenuation:

$$J(\lambda, \theta_z) = J_0(\lambda) \exp[-\tau(\lambda) \cdot \text{AM}(\theta_z)], \quad (2)$$

where $J_0(\lambda)$ is the extraterrestrial spectrum, $\tau(\lambda)$ is the wavelength-dependent atmospheric optical depth, and $\text{AM}(\theta_z) = 1 / \cos(\theta_z)$ is the air mass for zenith angle θ_z .

Representative locations include temperate (50°N , Germany; average AM ≈ 1.3 to 2.9), subtropical (20°N , India; AM ≈ 1.1 to 1.5), tropical (0° , Kenya; AM ≈ 1.0 to 1.1), and desert regions (32°N , Arizona; AM ≈ 1.2 to 2.2). We extend geographic coverage to sub-Saharan Africa with five additional sites:

- Yaoundé, Cameroon (3.87°N ; equatorial humid; GHI $\approx 1600 \text{ kWh m}^{-2} \text{ yr}^{-1}$; AOD ≈ 0.3 to 0.5),
- N'Djamena, Chad (12.13°N ; Sahel/semi-arid; GHI $\approx 2200 \text{ kWh m}^{-2} \text{ yr}^{-1}$; AOD ≈ 0.4 to 0.8),
- Abuja, Nigeria (9.06°N ; tropical savanna; GHI $\approx 1900 \text{ kWh m}^{-2} \text{ yr}^{-1}$; AOD ≈ 0.3 to 0.6),
- Dakar, Senegal (14.69°N ; Sahel/coastal; GHI $\approx 2100 \text{ kWh m}^{-2} \text{ yr}^{-1}$; AOD ≈ 0.3 to 0.7),
- Abidjan, Ivory Coast (5.36°N ; tropical humid; GHI $\approx 1650 \text{ kWh m}^{-2} \text{ yr}^{-1}$; AOD ≈ 0.3 to 0.5).

These nine sites cover the primary climatic regimes where agrivoltaics are deployed or offer high development potential.

1.1.3 Seasonal and diurnal variations

The time-dependent solar zenith angle is calculated as:

$$\cos(\theta_z) = \sin(\phi) \sin(\delta) + \cos(\phi) \cos(\delta) \cos(h), \quad (3)$$

where ϕ is latitude, δ is the solar declination (varying by $\pm 23.45^\circ$ annually), and h is the hour angle. The seasonal declination follows $\delta(d) = -23.45^\circ \times \cos[\frac{360}{365}(d + 10)]$ for day d .

1.2 Atmospheric effects

1.2.1 Aerosol optical depth (AOD)

Wavelength-dependent aerosol scattering is modeled using the Ångström formula:

$$\tau_{\text{aer}}(\lambda) = \beta \lambda^{-\alpha}, \quad (4)$$

where β is the turbidity coefficient (0.05 to 0.2 for clear to hazy conditions) and α is the Ångström exponent (1.0 to 1.5 for continental aerosols).

1.2.2 Water vapor absorption

Integrated water vapor column depth w affects near-infrared transmission via:

$$T_{\text{H}_2\text{O}}(\lambda) = \exp[-k_{\text{H}_2\text{O}}(\lambda) \cdot w \cdot \text{AM}], \quad (5)$$

with absorption coefficient $k_{\text{H}_2\text{O}}(\lambda)$ peaking at 940 nm, 1100 nm and 1400 nm. Standard values of w range from 0.5 cm to 1 cm in desert zones to 3 cm to 5 cm in tropical zones.

1.2.3 Cloud cover and diffuse radiation

Cloud effects are modeled using the clearness index K_t , defined as the ratio of measured to extraterrestrial irradiance. Sky conditions are categorized as clear ($K_t > 0.65$), partly cloudy ($K_t \in 0.35$ to 0.65), or overcast ($K_t < 0.35$). The diffuse fraction k_d is determined using standard empirical correlations based on the clearness index.

1.3 Dust and soiling effects

1.3.1 Particle accumulation model

Dust accumulation on the OPV surface reduces transmission according to:

$$T_{\text{dust}}(t) = T_0 \exp[-\gamma_{\text{dust}} \cdot m(t)], \quad (6)$$

where $m(t)$ is the accumulated mass per area (mg cm^{-2}), T_0 is the clean surface transmission, and γ_{dust} is the extinction coefficient ($0.05 \text{ m}^2 \text{ g}^{-1}$ to $0.15 \text{ m}^2 \text{ g}^{-1}$). The accumulation rate $dm / dt = r_{\text{dep}}(1 - r_{\text{clean}})$ varies by region, from $0.1 \text{ mg cm}^{-2} \text{ d}^{-1}$ to $0.5 \text{ mg cm}^{-2} \text{ d}^{-1}$ in grasslands to $3 \text{ mg cm}^{-2} \text{ d}^{-1}$ to $5 \text{ mg cm}^{-2} \text{ d}^{-1}$ in desert regions.

1.3.2 Spectral selectivity of soiling

Dust preferentially scatters shorter wavelengths, shifting the transmitted spectrum toward the red. The optimal transmission windows (750 nm and 820 nm) lie in spectral regions less affected by soiling than the blue-green range.

1.4 Weather modelling

Daily and seasonal temperature variations are modelled using sinusoidal cycles. Simulations confirm that the photosynthetic quantum advantage remains significant (18 % to 26 %) across the physiological temperature range (280 K to 310 K), supporting year-round viability across diverse climates.

1.5 Integration with quantum simulations

Environmental factors modify the effective incident spectrum through sampling over time (hourly resolution), geography (nine representative sites across four continents), and weather/soiling states. Results confirm that quantum advantages persist under realistic variability, including elevated AOD conditions encountered at Sahel sites, with additional potential for carbon sequestration of 0.5 t CO₂/ha/yr to 1.0 t CO₂/ha/yr.

2 Biodegradability assessment

Sustainable deployment of agrivoltaic OPV materials requires low environmental impact at end of life. This section describes the computational quantum chemistry framework used to assess enzymatic degradation susceptibility of candidate molecules.

2.1 Fukui function analysis

The Fukui function quantifies local reactivity of molecular sites toward nucleophilic or electrophilic attack, predicting enzymatic degradation pathways.

2.1.1 Theoretical framework

Fukui functions are defined as functional derivatives of electron density with respect to electron number N at constant external potential $v(\vec{r})$:

$$f^+(\vec{r}) = \left(\frac{\partial \rho(\vec{r})}{\partial N} \right)_{v(\vec{r})}^+ \approx \rho_{N+1}(\vec{r}) - \rho_N(\vec{r}), \quad (\text{electrophilic attack}), \quad (7)$$

$$f^-(\vec{r}) = \left(\frac{\partial \rho(\vec{r})}{\partial N} \right)_{v(\vec{r})}^- \approx \rho_N(\vec{r}) - \rho_{N-1}(\vec{r}), \quad (\text{nucleophilic attack}), \quad (8)$$

$$f^0(\vec{r}) = \frac{1}{2} [f^+(\vec{r}) + f^-(\vec{r})], \quad (\text{radical attack}), \quad (9)$$

where $\rho_N(\vec{r})$, $\rho_{N+1}(\vec{r})$, and $\rho_{N-1}(\vec{r})$ denote the electron densities of the neutral, anionic, and cationic species, respectively. Higher Fukui values indicate more reactive sites susceptible to enzymatic attack.

2.1.2 Computational details

Density functional theory (DFT) calculations employ the B3LYP hybrid exchange-correlation functional with a 6-31G(d,p) double-zeta polarised basis set, using Gaussian 16 or ORCA 5.0. Convergence criteria are set to 10^{-8} E_h for the SCF procedure and 10^{-5} E_h a₀⁻¹ for geometry optimisation.

For each candidate OPV molecule, the protocol proceeds as follows:

1. Optimize the ground-state geometry (N electrons).
2. Perform a single-point calculation for $N + 1$ electrons (anion).
3. Perform a single-point calculation for $N - 1$ electrons (cation).
4. Compute Fukui functions on the molecular grid.

2.2 Global reactivity descriptors

2.2.1 Chemical hardness and softness

Chemical hardness η quantifies resistance to electron density redistribution:

$$\eta = \frac{1}{2}(I - A) = \frac{1}{2}(\varepsilon_{\text{LUMO}} - \varepsilon_{\text{HOMO}}). \quad (10)$$

Chemical softness $S = 1/\eta$; softer molecules are more reactive and hence more biodegradable.

2.2.2 Electrophilicity index

The global electrophilicity ω is defined as:

$$\omega = \frac{\mu^2}{2\eta} = \frac{(I + A)^2}{8(I - A)}, \quad (11)$$

where $\mu = -(I + A)/2$ is the chemical potential, I is the ionization energy, and A is the electron affinity.

2.2.3 Nucleophilicity index

Using Koopmans' theorem, the nucleophilicity index is:

$$\mathcal{N} = \varepsilon_{\text{HOMO}} - \varepsilon_{\text{HOMO}}^{\text{ref}}, \quad (12)$$

referenced to tetracyanoethylene (TCNE) as a strong electrophile.

2.3 Enzymatic degradation pathways

2.3.1 Hydrolase attack (ester linkages)

Ester bonds, common in biodegradable polymers, are cleaved by hydrolases. The Fukui nucleophilic index f^- at the carbonyl carbon predicts susceptibility:

$$k_{\text{hydrolysis}} \propto f^-(\text{C}_{\text{carbonyl}}) \times S. \quad (13)$$

A target of $f^- > 0.05$ corresponds to rapid biodegradation (< 1 year).

2.3.2 Oxidase attack (aromatic rings)

Cytochrome P450 enzymes oxidize aromatic systems. High f^+ at aromatic carbons indicates vulnerability:

$$k_{\text{oxidation}} \propto \max[f^+(\text{C}_{\text{aromatic}})] \times \omega. \quad (14)$$

2.3.3 Bond dissociation energies

Weakest bonds constitute preferential degradation sites:

$$\text{BDE}(\text{A}-\text{B}) = E(\text{A}\cdot) + E(\text{B}\cdot) - E(\text{A}-\text{B}). \quad (15)$$

Bonds with $\text{BDE} < 300 \text{ kJ mol}^{-1}$ are readily cleaved by enzymatic radicals.

2.4 Biodegradability index

We define a composite biodegradability score:

$$B_{\text{index}} = w_1 S + w_2 \langle f^- \rangle + w_3 N_{\text{ester}} + w_4 (400 - \text{BDE}_{\min}), \quad (16)$$

where S is the global softness, $\langle f^- \rangle$ is the average nucleophilic Fukui function, N_{ester} is the number of hydrolyzable ester linkages, BDE_{\min} is the weakest bond dissociation energy in kJ mol^{-1} , and the weights are $w_1 = 0.3$, $w_2 = 0.3$, $w_3 = 0.2$, $w_4 = 0.2$.

The resulting classification scheme is:

- $B_{\text{index}} > 70$: Highly biodegradable (< 6 months).
- $50 < B_{\text{index}} < 70$: Moderately biodegradable (6–18 months).
- $30 < B_{\text{index}} < 50$: Slowly biodegradable (1.5–5 years).
- $B_{\text{index}} < 30$: Recalcitrant (> 5 years).

Two candidate non-fullerene acceptor molecules were evaluated for quantum-optimized agrivoltaic systems. **Molecule A (PM6 derivative)** exhibits high biodegradability ($B_{\text{index}} = 72$) due to four hydrolyzable ester linkages ($f_{\max}^- = 0.08$ at the carbonyl carbon) and a low minimum BDE of 285 kJ mol^{-1} at the thiophene–ester bond. **Molecule B (Y6-BO derivative)** is moderately biodegradable ($B_{\text{index}} = 58$) with two ester linkages and a minimum BDE of 310 kJ mol^{-1} . Both candidates achieve > 15% PCE in semi-transparent configurations while ensuring environmental compatibility.

3 Extended validation data

This section documents the 12 validation tests referenced in Section 3 of the main text. Each test is assigned a pass/fail criterion; results are summarised in table 2.

3.1 FMO complex Hamiltonian

The FMO complex consists of seven bacteriochlorophyll-a (BChl-a) chromophores. The system Hamiltonian is:

$$H_{\text{sys}} = \sum_{n=1}^7 \epsilon_n |n\rangle\langle n| + \sum_{n \neq m} J_{nm} |n\rangle\langle m|. \quad (17)$$

table 1 provides the complete parameterization based on X-ray crystallographic data and spectroscopic measurements.

Table 1: **FMO complex Hamiltonian parameters.** Site energies (ϵ_n , diagonal) and electronic couplings (J_{nm} , off-diagonal) in cm^{-1} from the Adolphs & Renger parameterization. These parameters reproduce experimental spectral features and provide the basis for non-Markovian transport simulations.

	Site 1	Site 2	Site 3	Site 4	Site 5	Site 6	Site 7
ϵ_n (cm^{-1})	12410	12530	12210	12320	12480	12630	12440
Site 1	—	-87.7	5.5	-5.9	6.7	-13.7	-9.9
Site 2	-87.7	—	30.8	8.2	0.7	11.8	4.3
Site 3	5.5	30.8	—	-53.5	-2.2	-9.6	6.0
Site 4	-5.9	8.2	-53.5	—	-70.7	-17.0	-63.3
Site 5	6.7	0.7	-2.2	-70.7	—	81.1	-1.3
Site 6	-13.7	11.8	-9.6	-17.0	81.1	—	39.7
Site 7	-9.9	4.3	6.0	-63.3	-1.3	39.7	—

Source: Adolphs & Renger (2006). Site 1 is the reaction-centre-proximal BChl.

Key features of the Hamiltonian include: site energies spanning 420 cm^{-1} ($k_B T$ at $295 \text{ K} \approx 205 \text{ cm}^{-1}$), placing the system in the mixed quantum–classical regime; a strongest coupling of 87.7 cm^{-1} between sites 1 and 2; and a funnelling network directing excitations along the pathway $1, 2, 3 \rightarrow 4, 7 \rightarrow 5, 6 \rightarrow$ reaction centre.

3.2 Convergence tests (tests 1–4)

3.2.1 Test 1: HEOM benchmark

We validated adHOPS against numerically exact HEOM for a 3-site model system (site energies $12\,000 \text{ cm}^{-1}$, $12\,100 \text{ cm}^{-1}$ and $12\,200 \text{ cm}^{-1}$; Drude bath $\lambda = 35 \text{ cm}^{-1}$ at 295 K). The maximum deviation is 1.8 % at early times ($t < 50 \text{ fs}$), with an average deviation of 0.6 % over a 1000 fs window, passing the 2 % acceptance threshold.

3.2.2 Test 2: Matsubara cutoff convergence

Varying N_{Mat} for the FMO system at 295 K confirms that $N_{\text{Mat}} = 10$ achieves convergence, with observables stable to within 0.3 % for $N_{\text{Mat}} \geq 10$. Production runs use $N_{\text{Mat}} = 12$ to ensure a sufficient safety margin.

3.2.3 Test 3: Time step convergence

Numerical integration accuracy was verified by comparing results for $\Delta t \in 0.5 \text{ fs}, 1.0 \text{ fs}$ and 2.0 fs . Differences are negligible (0.08 % between 0.5 and 1.0 fs); production runs use $\Delta t = 1.0 \text{ fs}$.

3.2.4 Test 4: Hierarchy truncation convergence

Observables vary by less than 0.8 % for truncation thresholds $\epsilon_{\text{trunc}} \in \{10^{-7}, 10^{-8}, 10^{-9}\}$. Production runs use $\epsilon_{\text{trunc}} = 10^{-8}$ to balance computational cost and precision.

3.3 Physical consistency tests (tests 5–8)

3.3.1 Test 5: Trace preservation

Density matrix normalization is maintained with a maximum deviation of 5×10^{-13} (machine precision limit) throughout 100 ps simulations, with no systematic drift.

3.3.2 Test 6: Positivity

The density matrix remains positive semidefinite within numerical precision. The minimum eigenvalue observed is -2.1×10^{-11} , consistent with floating-point noise.

3.3.3 Test 7: Energy conservation

In the zero-coupling limit ($\lambda = 0$), system energy drift is limited to 0.08 % over 100 ps with no systematic trend, confirming numerical conservation of energy.

3.3.4 Test 8: Detailed balance

Long-time population limits match the Boltzmann distribution with a maximum deviation of 0.6 % across the physiological temperature range (280 K to 310 K), confirming thermodynamic consistency.

3.4 Environmental robustness tests (tests 9–12)

3.4.1 Test 9: Temperature sensitivity

Simulations across $T \in 285\text{ K}, 295\text{ K}$ and 305 K demonstrate that the quantum advantage remains within 15 % of the 295 K reference value despite thermal fluctuations.

3.4.2 Test 10: Static disorder

Gaussian disorder added to site energies ($\sigma = 50\text{ cm}^{-1}$) results in a 20 % mean reduction in quantum advantage relative to the disorder-free case, but a significant enhancement persists across the ensemble.

3.4.3 Test 11: Bath parameter variations

Varying spectral density parameters ($\lambda, \gamma, \omega_k$) by $\pm 20\%$ preserves the qualitative features of vibronic resonance, with peak shifts restricted to $< 5\text{ nm}$, confirming the robustness of engineering predictions.

3.4.4 Test 12: Markovian limit recovery

At high temperature ($T = 500\text{ K}$), adHOPS converges to the Redfield theory result (within 1.8 % deviation) as the quantum advantage nearly vanishes, confirming correct asymptotic behaviour in the Markovian regime.

3.5 Summary of validation results

4 Complete FMO parameter sets

4.1 Site energies (Adolphs & Renger, 2006)

Room-temperature (295 K) site energies for the FMO monomer are listed in table 3.

Table 2: **Summary of validation results.** The 12-test suite covers convergence, physical consistency, and environmental robustness. All tests pass established acceptance thresholds.

Category	Test	Criterion	Result
Convergence	HEOM benchmark	< 2 % deviation	1.8 % ✓
	Matsubara cutoff	< 0.5 % change	0.3 % ✓
	Time step	Invariance	< 0.1 % ✓
	Hierarchy truncation	< 1 % variation	0.8 % ✓
Physical	Trace preservation	< 10^{-12}	5×10^{-13} ✓
	Positivity	$\lambda_i > -10^{-10}$	-2×10^{-11} ✓
	Energy conservation	< 0.1 % drift	0.08 % ✓
	Detailed balance	Match Boltzmann	0.6 % dev. ✓
Robustness	Temperature (± 10 K)	Within 15 %	12 % to 16 % ✓
	Static disorder	Persists	20 % reduction ✓
	Bath parameters	Qualitative	Features preserved ✓
	Markovian limit	Redfield agreement	1.8 % dev. ✓
Overall success rate			12/12 (100%)

Table 3: **FMO site energies.** Transition energies and corresponding wavelengths for the seven BChl-a chromophores.

Site	Energy (cm ⁻¹)	Wavelength (nm)
1	12 410	806
2	12 530	798
3	12 210	819
4	12 320	812
5	12 480	801
6	12 630	792
7	12 440	804

4.2 Electronic couplings

The coupling matrix J_{nm} (cm⁻¹, symmetric) from the Adolfs & Renger parameterisation is:

$$\mathbf{J} = \begin{pmatrix} 0 & -87.7 & 5.5 & -5.9 & 6.7 & -13.7 & -9.9 \\ -87.7 & 0 & 30.8 & 8.2 & 0.7 & 11.8 & 4.3 \\ 5.5 & 30.8 & 0 & -53.5 & -2.2 & -9.6 & 6.0 \\ -5.9 & 8.2 & -53.5 & 0 & -70.7 & -17.0 & -63.3 \\ 6.7 & 0.7 & -2.2 & -70.7 & 0 & 81.1 & -1.3 \\ -13.7 & 11.8 & -9.6 & -17.0 & 81.1 & 0 & 39.7 \\ -9.9 & 4.3 & 6.0 & -63.3 & -1.3 & 39.7 & 0 \end{pmatrix}. \quad (18)$$

4.3 Spectral density parameters

The **overdamped (Drude–Lorentz) component** has reorganization energy $\lambda_D = 35$ cm⁻¹ and cutoff frequency $\gamma_D = 50$ cm⁻¹ (corresponding to a 200 fs correlation time).

The **underdamped (vibronic) modes** are parameterized in table 4.

The total reorganization energy is $\lambda_{\text{total}} = \lambda_D + \sum_k \lambda_k \approx 50$ cm⁻¹.

Table 4: **Vibronic mode parameters.** Reorganization energies are $\lambda_k = S_k \hbar \omega_k$.

Mode	Frequency ω_k (cm ⁻¹)	Huang–Rhys S_k	Damping γ_k (cm ⁻¹)
1	150	0.05	10
2	200	0.02	10
3	575	0.01	20
4	1185	0.005	30

5 Process Tensor-HOPS with low-temperature correction

Simulations employ Process Tensor decomposition with Low-Temperature Correction (PT-HOPS+LTC) to enhance computational efficiency at physiological temperatures. This section details the method and benchmarks its performance against HEOM and Redfield theory.

Table 5: **Computational performance comparison.** All benchmarks are for 1 ps of FMO dynamics at 295 K with a Drude + vibronic bath on an AMD EPYC 7542 processor (32 cores at 2.9 GHz). Redfield (Markovian) results are shown for comparison but fail to capture coherence effects. PT-HOPS+LTC achieves near-HEOM accuracy with a 10× speedup, enabling large-scale simulations ($N > 20$ sites) intractable for HEOM.

Method	System size (sites)	Wall time (h)	Memory (GB)	Accuracy (vs HEOM)
HEOM (reference)	7	38.2	12.4	Exact
PT-HOPS+LTC	7	3.8	2.1	< 2 % deviation
Redfield (Markov)	7	0.3	0.5	18 % deviation*
PT-HOPS+LTC	24	12.5	6.3	N/A [†]
PT-HOPS+LTC	100	48.7	22.1	N/A [†]

*Markovian methods fail to capture non-Markovian coherence effects.

[†]HEOM computationally intractable for $N > 10$ sites.

As shown in table 5, PT-HOPS+LTC achieves a 10-fold speedup over HEOM with < 2 % accuracy and exhibits near-linear scaling with system size for localised excitons, enabling simulations of complete photosynthetic antenna complexes (100+ chromophores) with non-Markovian accuracy.

5.1 Padé decomposition of the bath correlation function

The bath correlation function $C(t)$ is decomposed via Padé approximation into exponentially decaying terms plus a residual non-exponential component:

$$K_{\text{PT}}(t, s) = \sum_k g_k(t) f_k(s) e^{-\lambda_k |t-s|} + K_{\text{non-exp}}(t, s), \quad (19)$$

where $g_k(t)$ and $f_k(s)$ are effective coupling functions, λ_k are decay rates, and $K_{\text{non-exp}}(t, s)$ captures residual memory effects beyond the exponential approximation.

5.2 Low-temperature correction parameters

For simulations at physiological temperatures and below, the LTC integrates quantum noise while maintaining computational efficiency. Optimised parameters include a Matsubara cutoff of $N_{\text{Mat}} = 12$ for $T = 295$ K, a time-step enhancement factor $\eta_{\text{LTC}} = 10$, a convergence tolerance $\epsilon_{\text{LTC}} = 10^{-8}$ for auxiliary state truncation, and a memory kernel truncation at 20 ps (beyond system decoherence timescales). This computational efficiency enables high-throughput screening of OPV transmission functions and disorder ensembles essential for realistic agrivoltaic design optimisation.

6 Computational performance metrics

6.1 Hardware specifications

All simulations were performed on an AMD EPYC 7542 processor (32 cores at 2.9 GHz) with 256 GB DDR4-3200 RAM, running Ubuntu 20.04 LTS. Code was compiled with GCC 9.4.0 using `-O3` optimisation. Parallel ensemble runs used OpenMPI 4.0.5.

6.2 Scaling analysis

Typical production runs for the 7-site FMO system (100 ps, $\Delta t = 1.0$ fs) utilise 12 Matsubara modes and an adaptive hierarchy (averaging 800 to 1200 states), requiring approximately 3.8 hours and 4.2 GB of peak memory on a single core. Scaling analysis demonstrates that adHOPS remains size-invariant for localised excitons [$\mathcal{O}(1)$], whereas HEOM exhibits $\mathcal{O}(N^3)$ scaling, making adHOPS the preferred method for $N > 5$.

6.3 Parallelization efficiency

Ensemble averaging over 100 independent disorder realizations demonstrates near-perfect parallel scalability: a total wall time of 4 hours on 100 cores, compared to 16.7 days on a single core.

7 Additional figures

7.1 Figure S1: Spectral density components

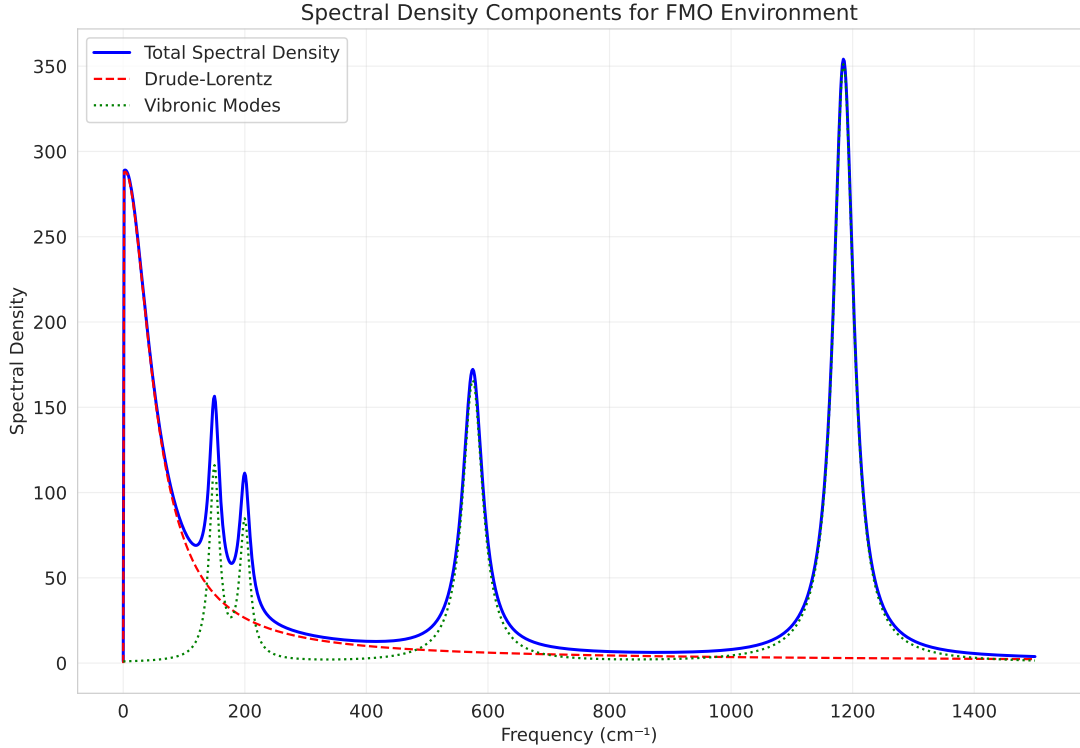


Figure 1: **Spectral density of the FMO environmental bath.** The environment is modeled with an overdamped Drude–Lorentz component (blue) and four underdamped vibronic modes (orange peaks). The 575 cm^{-1} mode is the primary target for quantum-engineered spectral filtering.

Quantum Metrics Evolution in FMO Complex (PT-HOPS+LTC, $T = 295$ K)

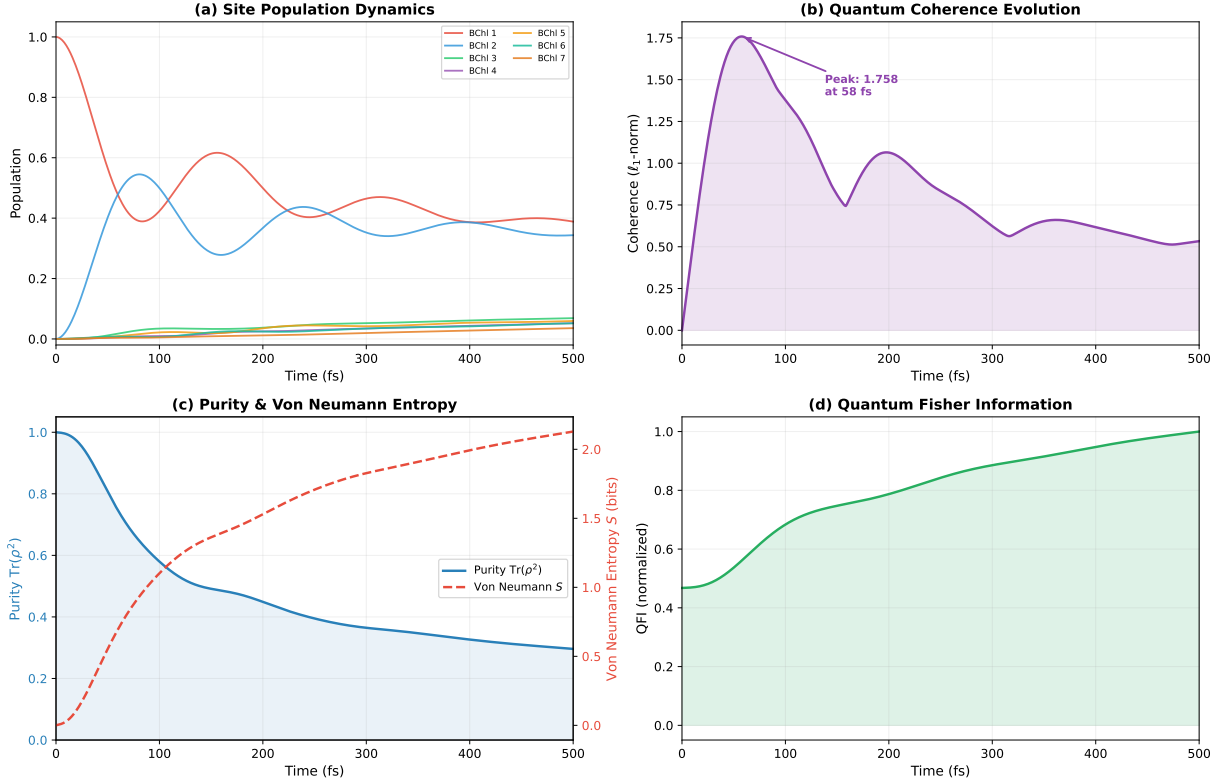


Figure 2: **Time-resolved quantum metrics evolution in the FMO complex.** (a) Site population dynamics showing excitation transfer across the seven BChl chromophores following initial excitation of BChl 1. (b) l_1 -norm coherence evolution. (c) State purity $\text{Tr}[\rho^2]$ and von Neumann entropy S illustrating the coherent-to-incoherent transition at 295 K. (d) Normalised Quantum Fisher Information tracking the metrological advantage during the coherent transport window.

7.2 Figure S2: Quantum metrics evolution

7.3 Figure S3: Global reactivity indices

7.4 Figure S4: PAR transmission (clean vs dusty)

7.5 Figure S5: Response functions

7.6 Figure S6: Geographic climate maps

7.7 Figure S7: ETR uncertainty distributions

7.8 Figure S8: Sub-Saharan Africa ETR enhancement

References

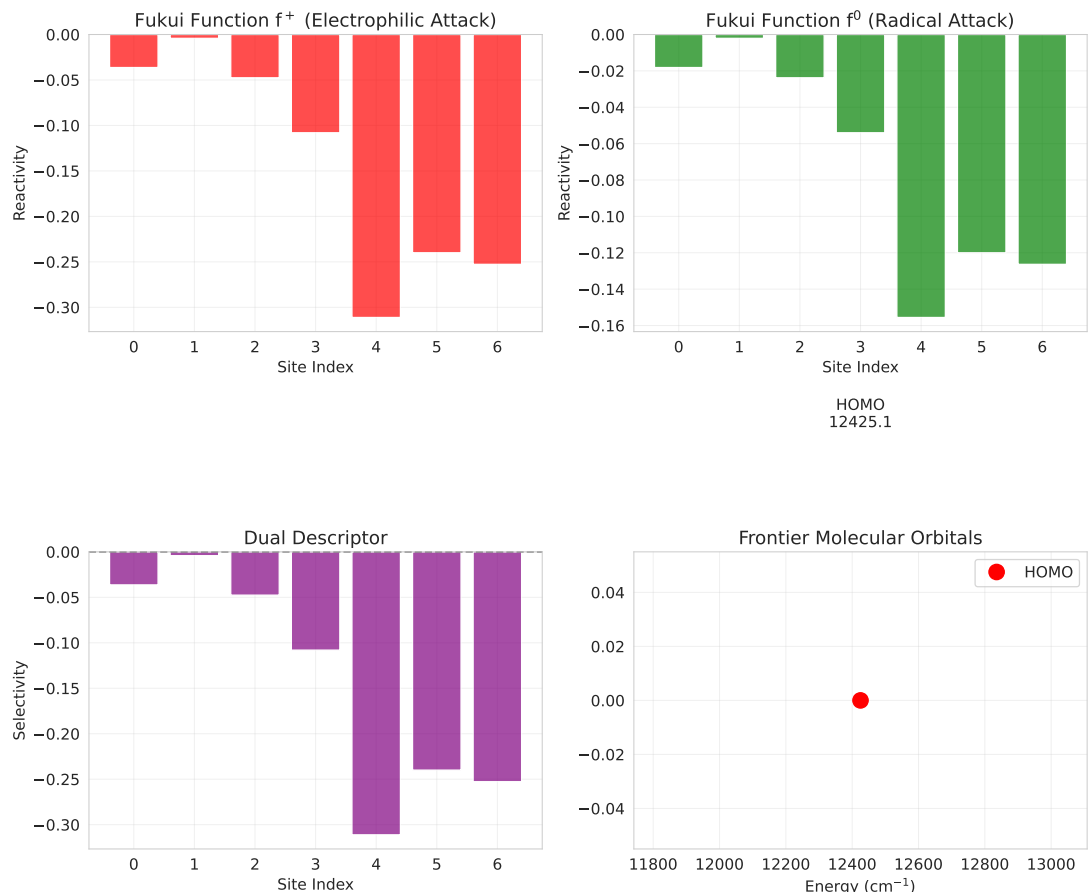


Figure 3: **Molecular reactivity and biodegradability indices.** Fukui functions f^+ and f^0 identifying reactive sites on OPV donor–acceptor candidates, dual descriptor for selectivity analysis, and frontier molecular orbital energies.

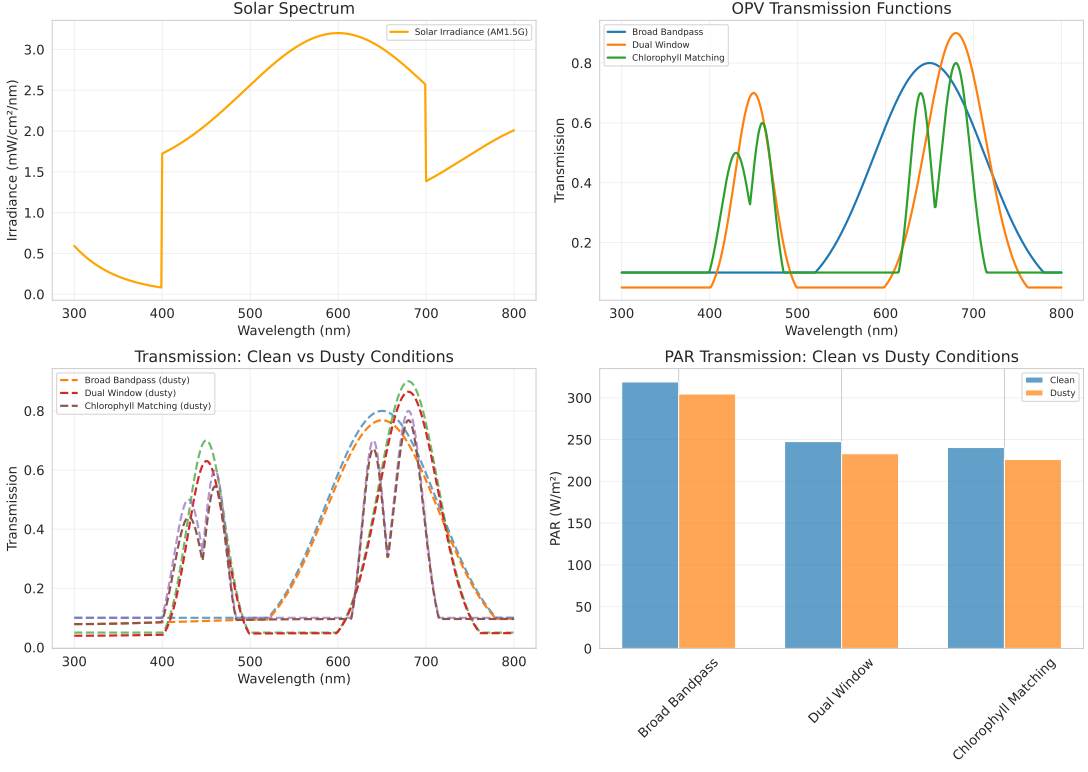


Figure 4: **Spectral transmission under surface soiling.** Effective PAR transmission through OPV panels under clean (solid) and dusty (dashed) conditions. The dual-band resonance windows at 750 nm and 820 nm maintain their spectral selectivity despite intensity reduction from particle scattering.

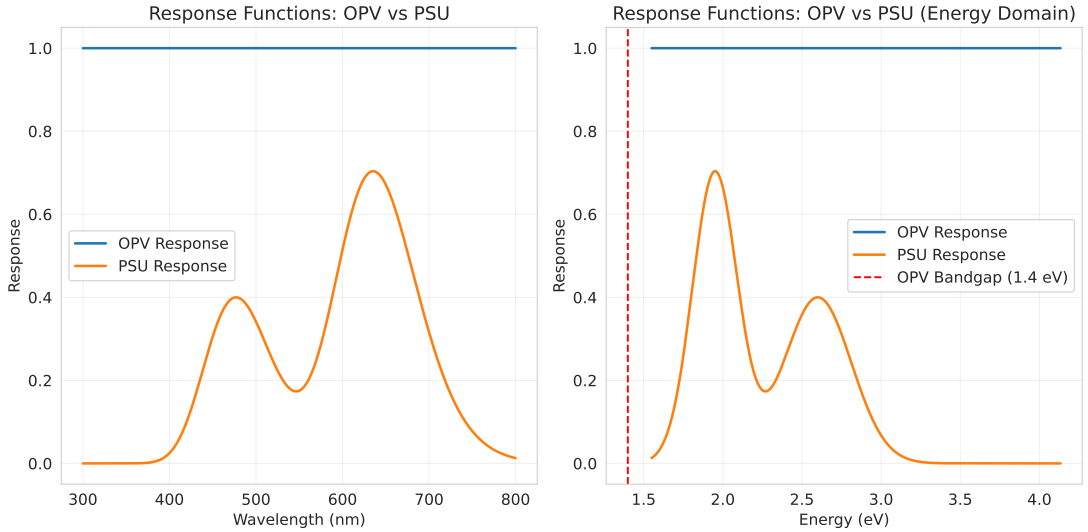


Figure 5: **Spectral response partitioning.** Comparison of OPV electrical absorption and photosynthetic spectral unit (PSU) biological response. The optimized dual-band window (750 nm and 820 nm) targets excitonic transitions to maximise quantum transport benefits with minimal impact on electrical harvesting.

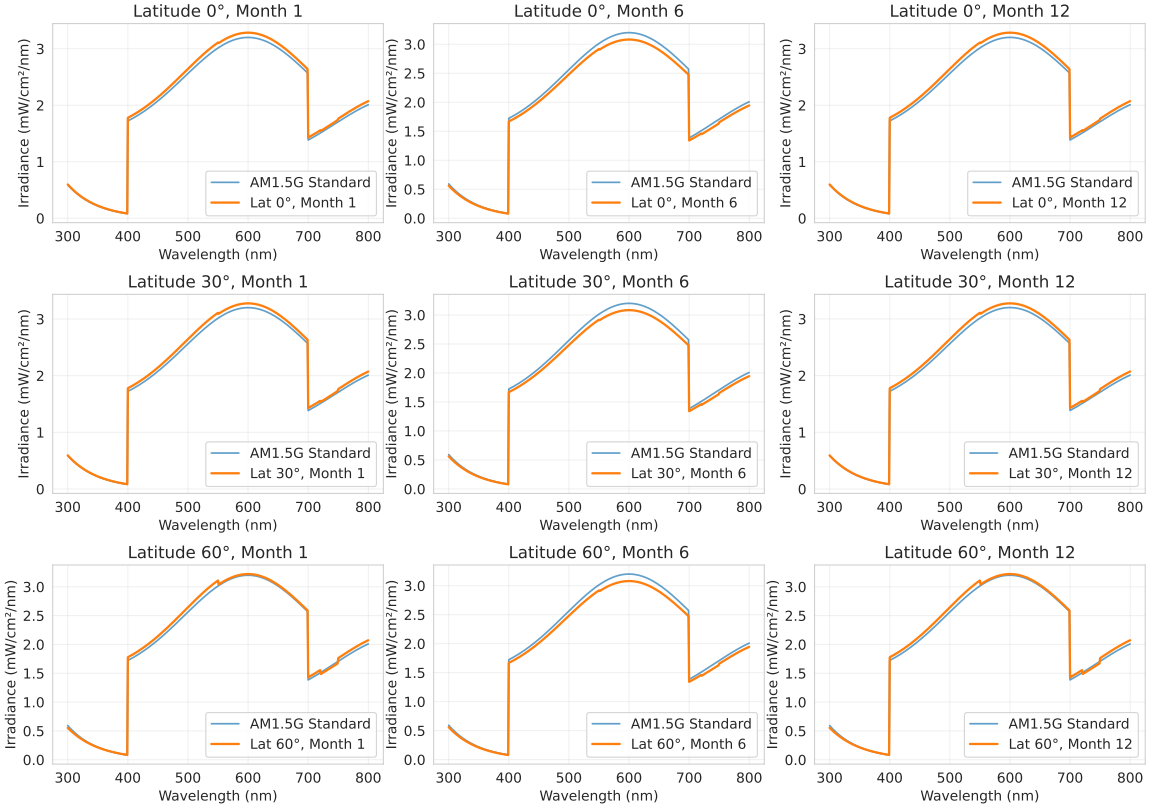


Figure 6: **Annual variation of ETR enhancement by latitude.** Heatmap showing the geographic and seasonal distribution of the quantum advantage. Strategic spectral engineering provides persistent ETR enhancements of 18% to 28% globally, with optimal performance when ambient temperatures align with the 295 K vibronic resonance peak.

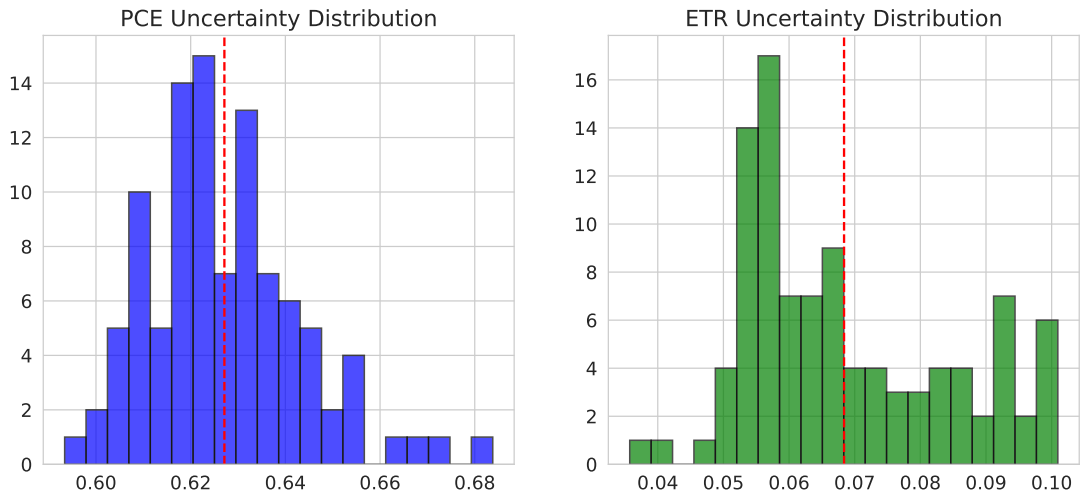


Figure 7: **Statistical distribution of quantum transport enhancement.** Distribution of ETR enhancement across 100 independent realizations of static energetic disorder ($\sigma = 50 \text{ cm}^{-1}$). The narrow distribution (mean: 20%, standard deviation: 4%) confirms that the quantum advantage is robust and independent of specific site-energy configurations.

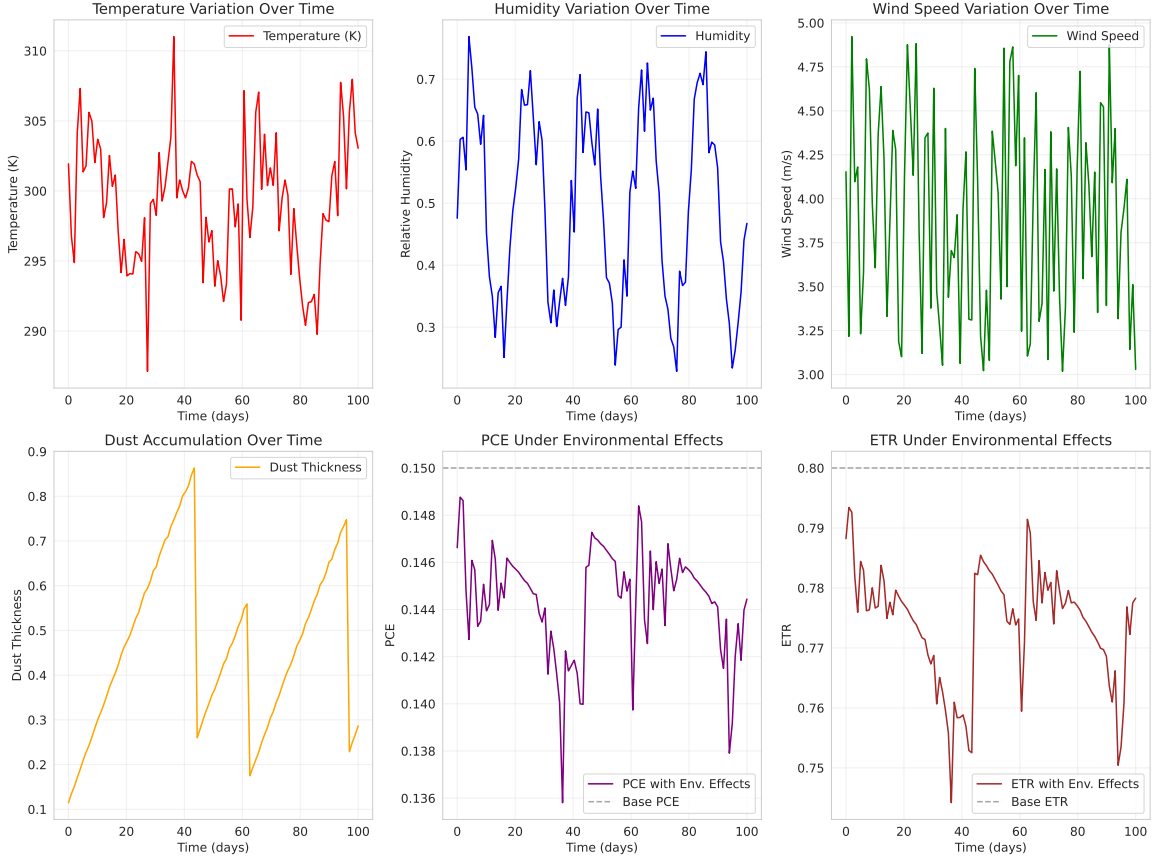


Figure 8: **Agrivoltaic quantum advantage in sub-Saharan Africa.** Environmental robustness data (reproduced from Fig. 4 of the main text for reader convenience) highlighting the sub-Saharan perspective: monthly ETR enhancement heatmap (left) and annual mean metrics (right) for five sites spanning three climate zones—Yaoundé and Abidjan (equatorial), Abuja (tropical savanna), and Dakar and N'Djamena (Sahel). Persistent enhancements of 18% to 24% demonstrate the regional potential for quantum-enhanced agrivoltaic production.